Available online at www.sciencedirect.com
SCIENCE DIRECT®
Journal of Computational Physics 208 (2005) 154–174
JOURNAL OF COMPUTATIONAL PHYSICS
www.elsevier.com/locate/jcp

High order Godunov mixed methods on tetrahedral meshes for density driven flow simulations in porous media

Annamaria Mazzia, Mario Putti *

Department of Mathematical Methods and Models for Scientific Applications, University of Padua, via Belzoni 7, 35131 Padova, Italy

Received 7 October 2004; received in revised form 25 January 2005; accepted 26 January 2005
Available online 14 April 2005

Abstract

Two-dimensional Godunov mixed methods have been shown to be effective for the numerical solution of density-dependent flow and transport problems in groundwater even when concentration gradients are high and the process is dominated by density effects. This class of discretization approaches solves the flow equation by means of the mixed finite element method, thus guaranteeing mass conserving velocity fields, and discretizes the transport equation by mixed finite element and finite volumes techniques combined together via appropriate time splitting. In this paper, we extend this approach to three dimensions employing tetrahedral meshes and introduce a spatially variable time stepping procedure that improves computational efficiency while preserving accuracy by adapting the time step size according to the local Courant–Friedrichs–Lewy (CFL) constraint. Careful attention is devoted to the choice of a truly three-dimensional limiter for the advection equation in the time-splitting technique, so that to preserve second order accuracy in space (in the sense that linear functions are exactly interpolated). The three-dimensional Elder problem and the salt-pool problem, recently introduced as a new benchmark for testing three-dimensional density models, provide assessments with respect to accuracy and reliability of this numerical approach.

Keywords: Coupled flow and transport equations; High order finite volume; Mixed hybrid finite element; Time splitting; Tetrahedral mesh

1. Introduction

The study of coupled flow and transport problems in porous media has received growing interest in the last few years within the specialized literature. In particular, the recent development of efficient numerical

* Corresponding author. Tel.: +390498275919; fax: +390498275995.
E-mail address: putti@dmsa.unipd.it (M. Putti).

0021-9991/$ - see front matter © 2005 Elsevier Inc. All rights reserved.
doi:10.1016/j.jcp.2005.01.029

techniques and of fast and easily available computational tools has promoted a number of studies concerning the modeling aspects of the phenomenon [1–4]. The occurrence of local recirculation patterns due to the density differences that appear in the presence of dissolved salts in the groundwater renders the coupled flow and transport equations nonlinear and contributes to the difficulties encountered in the numerical simulations of this type of problems.

Recently developed well-controlled lab experiments [5–7] have contributed to the understanding of the physical phenomenon and have prompted the use of these solutions as benchmark test cases for numerical simulators. A recent review on these aspects [8] and a few significant applications [9,10] have shown that the correct accuracy and reliability of the numerical solutions may not be rapidly attainable. In particular, in the case of three-dimensional simulations, the numerical difficulties may easily become overwhelming. For this reason accurate and stable algorithms need to be devised.

When using standard finite element schemes, a common approach in the hydrological community, a number of drawbacks and inaccuracies arise, in particular in the calculation of velocities when unstructured grids are employed [11]. On the other hands, block centered finite differences or finite volumes can be shown to be equivalent to the mixed finite element approach on regular meshes [12]. In this paper, we describe the development of a three-dimensional numerical scheme based on the mixed hybrid finite element (MHFE) method for the discretization of the flow equation and a combination of MHFE with high resolution finite volumes (HRFV) via a time-splitting technique [13,14] for the discretization of the transport equation. This procedure has been shown to be an effective tool for the solution of the coupled flow and transport problem in two dimensions [15,9,16]. It has been applied to Elder's problem, showing its accuracy and reliability without suffering from numerical oscillations but still introducing only a minimum amount of numerical diffusion. The two-dimensional version of this approach was used in [9] to solve the salt lake problem, introduced by [17] as a test case for density-dependent groundwater flow and solute transport. Moreover, it has been applied for high-concentration brine transport [16] following the nonlinear dispersion law proposed by [18,19]. The reasons for the success of this approach are twofold. First the MHFE scheme applied to the flow equation yields a discrete velocity field with normal components that are continuous across interelement boundaries. This property guarantees that no mass balance errors due to numerical inaccuracies in the flow discretization are introduced in the solution of the transport equation. The second reason is related to the HRFV method used in the approximation of the convective fluxes. This technique is capable of capturing sharp fronts and to accurately follow their dynamics, a characteristic of fundamental importance for density driven flows.

The full transport equation is solved by means of a time-splitting approach that combines the MHFE discretizing the dispersion fluxes and HRFV for the convective fluxes. Since integration in time is explicit for HRFV, thus requiring time step size restrictions according to the CFL constraint, and implicit for MHFE, different time steps are allowed for advection and dispersion. It has been observed that some simulation runs require very long computing times, due to the extremely small advective time steps resulting from the presence of large velocities combined with small cell sizes in only small parts of the domain. This phenomenon suggests the use of space variable time step sizes for the time-splitting technique. A similar procedure was described and analyzed in [20] on two-dimensional rectangular meshes. In this paper, we describe how such a technique can be effectively implemented in a three-dimensional solver to achieve high computational performance.

When extending the time-splitting technique to three dimensions, particular attention has to be devoted to the choice of a truly three-dimensional limiter for the advection equation. Interpolation on uniform or rectangular meshes does not pose serious problems in the reconstruction phase. On the other hand, when working on unstructured tetrahedral meshes, it is difficult to maintain high accuracy for all cell configurations [21]. For this reason we perform a numerical comparison of the behavior of several reconstruction-limiter combinations using a simple linear advection equation. Verification of the achievement of superlinear global convergence (close to second order) is studied by solving simple multiple dimensional

linear advection equations. Indeed, several generalization of two-dimensional HRFV schemes do not preserve spatial second order of accuracy due to the poorly structured tetrahedra that need to be used in a three-dimensional mesh; on the contrary, other schemes seem to be well suited for application to tetrahedra [22]. The reconstruction chosen for the FV scheme is based on the limiter proposed by [21]. As usual, when dealing with finite volume methods, there is the choice of working with cell or node based schemes [23]. We use the former approach because of the need of preserving compatibility with the MHFE approach used to discretize dispersion. Thus we consider here three-dimensional extensions of the reconstruction-limiter couples proposed in [24–27,21]. Our aim is to maintain simplicity and robustness in the overall scheme, and for this reason we do not consider in this work the class of diamond schemes as proposed in [28] and analyzed in [29]. Also ENO type schemes [30,31] are not investigated in this paper as the use of a variable stencil complicates the coupling with MHFE.

The extended procedure for the numerical solution of coupled flow and transport problems is tested on the three-dimensional Elder problem [32] and on the saltpool problem, a three-dimensional benchmark test introduced recently by [7,10]. Both test cases are useful to describe the performance of the proposed approach and to discuss some challenging issues related to density-dependent flow in porous media.

2. Governing equations

The mathematical model of density-dependent flow and transport in groundwater [33] can be expressed in terms of an equivalent freshwater head h defined as $h = \psi + z$, where $\psi = p/(\rho_0 g)$ is the equivalent freshwater pressure head, p is the pressure, ρ_0 is the freshwater density, g is the gravitational constant, and z is the vertical coordinate directed upward. The density ρ of the saltwater solution is written in terms of the reference density ρ_0 and the normalized (actual divided by maximum) salt concentration c:

$$\rho = \rho_0(1 + \epsilon c), \tag{1}$$

where $\epsilon = (\rho_s - \rho_0)/\rho_0$ is the density ratio and ρ_s is the density of the solution at $c = 1$. The dynamic viscosity μ of the saltwater mixture is also expressed as a function of c and of the reference viscosity μ_0 as

$$\mu = \mu_0(1 + \epsilon' c), \tag{2}$$

where $\epsilon' = (\mu_s - \mu_0)/\mu_0$ is the viscosity ratio and μ_s is the viscosity of the solution at $c = 1$.

With the above definitions, the mass conservation equations for the coupled flow and transport model in porous media can be written as [4]:

$$\sigma \frac{\partial \psi}{\partial t} = \vec{\nabla} \cdot \left[K_s \frac{1 + \epsilon c}{1 + \epsilon' c} (\vec{\nabla} \psi + (1 + \epsilon c)\vec{\eta}_z) \right] - \phi \epsilon \frac{\partial c}{\partial t} + \frac{\rho}{\rho_0} q^* + q, \tag{3}$$

$$\vec{v} = -K_s \frac{1 + \epsilon c}{1 + \epsilon' c} (\vec{\nabla} \psi + (1 + \epsilon c)\vec{\eta}_z), \tag{4}$$

$$\phi \frac{\partial c}{\partial t} = \vec{\nabla} \cdot (D \vec{\nabla} c) - \vec{\nabla} \cdot (c\vec{v}) + q c^* + f, \tag{5}$$

where t is time, $\sigma = S_s(1 + \epsilon c)$ is the general storage term, S_s is the storage coefficient, $\vec{\nabla}$ is the gradient operator, K_s is the hydraulic conductivity tensor at the reference density defined as $K_s = \rho_0 g k/\mu_0$ with k the intrinsic permeability, $\vec{\eta}_z$ is a vector equal to zero in its x and y components and 1 in its z component, ϕ is the porosity of the medium, q^* is the injected and q the extracted volumetric flow rate, $\vec{v}$ is the Darcy velocity vector, D is the dispersion tensor, given by [33] as $D = (\phi D_0 + \alpha_T |\vec{v}|) I + (\alpha_L - \alpha_T) \vec{v} \cdot \vec{v}^T / |\vec{v}|$, with D_0 the molecular diffusion coefficient and α_L and α_T the longitudinal and transverse dispersivities, c^* is

the normalized concentration of salt in the injected/extracted fluid, and f is the volumetric rate of injected (positive)/extracted (negative) solute that does not affect the velocity field. Appropriate initial and Dirichlet, Neumann, or Cauchy boundary conditions are added to complete the mathematical formulation of the flow and transport problem.

Note that, if we neglect molecular diffusion, the dispersion tensor D represents the effects of contaminant mixing due to the pore-scale heterogeneity of the local velocity field. Mathematically, it is equivalent to a diffusion term and thus multiplies the concentration gradient in the mass balance equation (5) [33,34].

3. Numerical discretization

The numerical approach used to solve the coupled flow and transport equation extends to three dimensions the procedure successfully applied in two dimensions [9,16]. The aim is to obtain accurate and monotone solutions in both velocity and concentration fields, also when the transport equation is advection dominated. For this reason the flow equation is discretized by means of a MHFE approach that yields the best compromise between accuracy and performance. The algorithm employed in this work is a three-dimensional extension of the scheme described in [13,35], and uses the RT0 functional spaces defined on tetrahedra.

The transport equation is first split into a dispersion and an advection equations. These are then discretized by implicit MHFE and explicit cell-centered Godunov-like finite volume schemes, respectively. The two discretizations are combined together via an appropriate time-splitting technique [13] that achieves second order accuracy if the time-step size used in the dispersion step is the same as the one used in the advection step [14]. The time-splitting approach employed here has been thoroughly discussed in its two-dimensional version in [13–15] and successfully applied to density-dependent porous media flow in [9,16]. Extensions to tetrahedra are reported in [36].

The solution of the nonlinear system of equations arising from the discretization of the flow and transport equations is addressed with an iterative Picard-like scheme as described in [9] by which the problem is decoupled by first solving the flow equation, then calculating the velocity field, and finally solving the transport equation. This three-step sequence is repeated until convergence.

Application of the MHFE to three-dimensional triangulations is just a straightforward extension of the two-dimensional case. For details about the implementation see [35], and this holds true for both the flow equation and the dispersion term in the transport equation. Implementation of the finite volume approach to unstructured tetrahedral meshes possess higher difficulties in the reconstruction phase but most importantly in the definition of an appropriate fully three-dimensional limiter. For this reason in the following we refer to the literature for the MHFE, e.g. [37], while we report a more detailed discussion on the choices made for the Godunov-like finite volume scheme.

Let $\mathscr{T}_h$ be a triangulation of the domain $\Omega \in \mathbb{R}^3$ and let T_l be a generic cell (tetrahedron) of $\mathscr{T}_h$. Recall that, since ϕ is constant in time, Eq. (5), over the time interval $[t^k, t^{k+1}]$ with time step Δt, may be written in semi-discrete form as:

$$\phi_l c_l^{k+1} = \phi_l c_l^k - \frac{\Delta t}{|T_l|} \int_{T_l} [\vec{\nabla} \cdot (\vec{F}(c^{k+1-\theta}) + \vec{G}(c^{k+\theta})) - f^{k+\theta}] \, \mathrm{d}\Delta, \quad l = 1, \ldots, m \tag{6}$$

where ϕ_l is the value of porosity in the centroid of T_l, k is the time step index, c_l^k is the volume average over T_l with $|T_l|$ being the volume of T_l, $\vec{F} = c\vec{v}$ is the advective flux, $\vec{G} = -D\vec{\nabla} c$ is the dispersive flux and $f^{k+\theta}$ contains the terms qc^* and f. A weighted scheme is used for the time quadrature with weighting parameter $\theta \in [0.5, 1]$. Integration in time is explicit for the HRFV scheme and implicit for the MHFE method. We

combine explicit and implicit first order Euler scheme ($\theta = 1$) or explicit and implicit second order midpoint rule ($\theta = 0.5$).

3.1. The finite volume approach on tetrahedra

The advection equation extracted from (6) can be explicitly written as:

$$\phi_l c_l^{k+1} = \phi_l c_l^k - \frac{\Delta t}{|T_l|} \int_{T_l} \vec{\nabla} \cdot \vec{F}(c_l^{k+1-\theta})\, \mathrm{d}\Delta \tag{7}$$

with $l = 1, \ldots, m$.

Two-dimensional finite volume scheme on unstructured triangular grid, as developed by [24] and then modified by [38], can be theoretically generalized to tetrahedra. In practice, we observe that direct extension of many two-dimensional limiters may drastically reduce the order of accuracy and yield poor results. The reason for this behavior is mainly attributed to interpolation errors that arise in the presence of poorly structured tetrahedra that generally form a three-dimensional triangulation [22,36]. More in detail, application of the divergence theorem to the right-hand side of (7) yields

$$\phi_l c_l^{k+1} = \phi_l c_l^k - \frac{\Delta t}{|T_l|} \sum_{j=1}^{4} \int_{e_{lj}} \vec{F}(c_l^{k+1-\theta}) \cdot \vec{n}_{lj}\, \mathrm{d}\Gamma, \tag{8}$$

where e_{lj}, $j = 1, 2, 3, 4$ are the faces of tetrahedron T_l and $\vec{n}_{lj}$ are the corresponding (outward) unit normals. The approximation of the four integrals (advective fluxes) in the above equation is achieved by introducing the numerical flux H_{lj}^{G}:

$$\phi_l c_l^{k+1} = \phi_l c_l^k - \frac{\Delta t}{|T_l|} \sum_{j=1}^{4} H_{lj}^{\mathrm{G}}, \tag{9}$$

where H_{lj}^{G} is the two-point Lipschitz monotone flux (the Godunov flux) that depends on the cell averaged values of the concentration variable evaluated on the right and left sides of face e_{lj}, $j = 1, \ldots, 4$ at time $t^{k+1-\theta}$ (for clarity we omit when unnecessary the time index k). The flux H_{lj}^{G} can be defined as:

$$H_{lj}^{\mathrm{G}} = H(c_{\mathrm{R}j}, c_{\mathrm{L}j}, n_{lj}) \bar{T}_{lj}, \tag{10}$$

where $c_{\mathrm{R}j}$ and $c_{\mathrm{L}j}$ are the reconstructed values c on the right and left sides of face e_{lj} of T_l, and $\bar{T}_{lj}$ is the surface area of face e_{lj}.

To obtain second order approximation in space, $c_{\mathrm{R}j}$ and $c_{\mathrm{L}j}$ are linearly reconstructed component-wise from the cell averaged data:

$$c_{Xj} = \left[c_l + \vec{r}_{lj} \cdot \vec{\nabla}(L_l) \right]_X, \quad X = \mathrm{R}, \mathrm{L}, \tag{11}$$

where $\vec{r}_{lj}$ is the vector from the centroid of cell T_l to the centroid of the face e_{lj} and $\vec{\nabla}(L_l)$ is the gradient of a linear polynomial L_l defined on T_l. A second order accurate method is thus achieved in the sense that a linear solution is modeled exactly, but overshoots and undershoots at the centroids of the tetrahedra faces may be introduced. Non-linear correction factors called 'limiters' are employed to avoid these oscillations and to satisfy a local maximum principle. These limiters must be designed so that global second order accuracy is not destroyed, i.e., they have to add corrections to the interpolation (11) that act only locally in the presence of sharp gradient changes or local extrema. As we will see, a careful definition of this limiting function is crucial to achieve the full potential of the method.

3.2. Three-dimensional reconstruction and limiting

In this section, we describe several three-dimensional reconstructions and corresponding limiters that are applicable to tetrahedral meshes. Some are extensions of two-dimensional techniques, others have been proposed expressively for tetrahedra.

3.2.1. The DUR approach

The three-dimensional extension of the scheme developed by [24], denoted from now on as the DUR approach, can be obtained as follows. In each tetrahedron, four hyperplanes, L_l^j, $j = 1,2,3,4$, can be constructed by interpolating the concentration values at the centroid $\vec{P}_l$ of the reference tetrahedron and the centroides $\vec{P}_p$, $\vec{P}_q$, $\vec{P}_r$, $\vec{P}_s$ of its four neighbors, T_p, T_q, T_r, T_s. If a face e_i of T_l is a boundary face, we use $(\vec{P}_{li}, c(\vec{P}_{li}, t))$ instead of $(\vec{P}_p, c_p)$ to build the linear interpolation, where $\vec{P}_{li}$ is the centroid of face e_i. Next, we compute the Euclidean norm of the gradient of each L_l^j:

$$|\vec{\nabla}(L_l^j)| = \sqrt{\left(\frac{\partial L_l^j}{\partial x}\right)^2 + \left(\frac{\partial L_l^j}{\partial y}\right)^2 + \left(\frac{\partial L_l^j}{\partial z}\right)^2} \quad j = 1,2,3,4.$$

Starting form the L_l^j with maximum gradient and going toward the L_l^j with minimum gradient, we choose the first j that satisfies:

$$\begin{aligned} &L_l^j(\vec{P}_{lp}) \text{is between } c_l \text{ and } c_p, \\ &L_l^j(\vec{P}_{lq}) \text{is between } c_l \text{ and } c_q, \\ &L_l^j(\vec{P}_{lr}) \text{is between } c_l \text{ and } c_r, \\ &L_l^j(\vec{P}_{ls}) \text{is between } c_l \text{ and } c_s, \end{aligned} \tag{12}$$

where $\vec{P}_{lp}$ is the centroid of the face sharing T_l and T_p tetrahedron, and so on. If no L_l^j satisfies the requirements (12), we choose $L_l = c_l$, that is first order reconstruction.

From a theoretical point of view, the properties of DUR in two dimensions should be readily generalized to tetrahedra. In practice, the extension of the limiter to three dimensions may reduce the observed order of accuracy. The great computational effort needed to choose the right interpolant for the linear reconstruction does not correspond to an improvement in terms of accuracy of the solution. Even if it has been noted that the use of linear reconstructions does not always imply second or higher order accuracy also when the solution is smooth [21], such failure requires more investigation. Indeed, a similar behavior is observed also for other two-dimensional schemes extended to tetrahedra [25,26,30].

3.2.2. The MIN approach

The *min* limiter (MIN) is discussed in [24] as a procedure analogous to the *min* limiter in second order ENO (essentially non-oscillatory) schemes [30]. It corresponds to the selection of the interpolant with minimum gradient, among the four DUR candidates. At the extrema, that is when concentration is an extremum relative to the values of c at the centroids of the neighboring tetrahedra, a first order approximation is used.

3.2.3. The LCD approach

The limited central difference (LCD) scheme is presented in [25] for unstructured triangular meshes. Its extension to three dimensions is obtained by constructing the plane that interpolates concentration values at the centroids of the four neighboring elements. Limiting is performed as follows. Let L_l^5 be the interpolant of the four pairs of points and corresponding concentration values

$$(\vec{P}_p, c_p)(\vec{P}_q, c_q)(\vec{P}_r, c_r)(\vec{P}_s, c_s).$$

The LCD scheme limits L_l^5 by setting

$$\alpha^v = \begin{cases} \frac{\max(c_v - c_l, 0)}{\vec{r}_{lv} \cdot \vec{\nabla}(L_l^5)} & \text{if } \vec{r}_{lv} \cdot \vec{\nabla}(L_l^5) > \max(c_v - c_l, 0), \\ \frac{\min(c_v - c_l, 0)}{\vec{r}_{lv} \cdot \vec{\nabla}(L_l^5)} & \text{if } \vec{r}_{lv} \cdot \vec{\nabla}(L_l^5) < \min(c_v - c_l, 0), \\ 1 & \text{otherwise,} \end{cases} \quad v = p, q, r, s,$$

where $\vec{r}_{lv}$ is the vector from the centroid of T_l to the centroid of the face between cells T_l and T_v. The LCD gradient operator is then calculated as

$$L_l = \alpha L_l^5 = \min_{v=p,q,r,s} \alpha^v L_l^5.$$

3.2.4. The MLG approach

The maximum limited gradient (MLG) scheme is proposed in [26] and can be described as a combination of the methodologies proposed for the DUR and LCD schemes. It takes all five linear interpolants (the candidates for the reconstruction of the DUR and the LCD), limits each one in turn in the manner of the LCD scheme and chooses the remaining operator with largest gradient.

3.2.5. The LSM approach

The above methods, applied in three dimensions, appear inadequate to achieve full accuracy. On the contrary, other schemes seem to be better suited to be applied on tetrahedra. The linear interpolant is the least squares approximation of the centroid values of the reference tetrahedron and its four neighbors. The procedure is less expensive than the methods that require the definition of four or more linear interpolants, and, at the same time, takes into account the full information available in the reference tetrahedron and its neighbors.

The least square method minimizes the functional

$$S(L_l) = \sum_{v \in \{l,p,q,r,s\}} (L_l(\vec{P}_v) - c_v)^2, \tag{13}$$

where l and p, q, r, s represent the tetrahedron and its four neighbors, respectively. The gradient $\vec{\nabla}(L_l)$ is then the slope of the resulting hyperplane.

The extremum limiter (LSM_EXTR) does not limit the gradients but directly the values of the variables on both sides of the face. It can be formulated [27] as:

$$\Phi = \begin{cases} 0 & \text{if } \min(c_l, c_v) \leqslant c_{lv}^{\text{old}} \leqslant \max(c_l, c_v), \\ \max(c_l, c_v) - c_{lv}^{\text{old}} & \text{if } c_{lv}^{\text{old}} > \max(c_l, c_v), \\ \min(c_l, c_v) - c_{lv}^{\text{old}} & \text{if } c_{lv}^{\text{old}} < \min(c_l, c_v). \end{cases}$$

The limited value of c_{lv} is given by:

$$c_{lv} = c_{lv}^{\text{old}} + \Phi, \quad v = p, q, r, s,$$

where

$$c_{lv}^{\text{old}} = c_l + \vec{r}_{lv} \cdot \vec{\nabla}(L_l), \quad v = p, q, r, s. \tag{14}$$

The last method in this comparison, the LSM_BJ method, applies the slope limiter by computing [21]

$$c_{lv} = c_l + \Phi_l \vec{r}_{lv} \cdot \vec{\nabla}(L_l), \quad v = p, q, r, s, \tag{15}$$

where $\Phi_l = \min(\Phi_{lp}, \Phi_{lq}, \Phi_{lr}, \Phi_{ls})$ and

$$\Phi_{lv} = \begin{cases} 1 & \text{if } c_{lv}^{\text{old}} - c_l = 0, \\ \min\left(1, \frac{(c_l^{\max} - c_l)}{(c_{lv}^{\text{old}} - c_l)}\right) & \text{if } c_{lv}^{\text{old}} - c_l > 0, \\ \max\left(1, \frac{(c_l^{min} - c_l)}{(c_{lv}^{\text{old}} - c_l)}\right) & \text{if } c_{lv}^{\text{old}} - c_l < 0. \end{cases} \tag{16}$$

In the previous formula, $c_l^{\min} = \min(c_l, \min_v^4 c_v)$ and $c_l^{\max} = \max(c_l, \max_v c_v)$. The application of this slope limiter guarantees that a local maximum principle condition is satisfied [21].

3.3. Numerical comparison of the different reconstruction-limiter combinations

The choice of the most appropriate reconstruction-limiter combination is based mainly on accuracy and convergence properties of the overall algorithm. Numerical assessment of these characteristics is performed by solving in one and two spatial dimensions the advection equation whose exact solutions are $x - v_x t$ (TEST1A), $\sin 2\pi(x - v_x t)$ (TEST1B), and $\sin 2\pi(x - v_x t)\sin 2\pi(y - v_y t)$ (TEST2). Appropriate Dirichlet boundary conditions and velocity equal to $\vec{v} = (1, 0, 0)$ for the one-dimensional tests and to $\vec{v} = (1, 1, 0)$ for the two-dimensional example are imposed.

Numerical convergence of the different FV schemes is evaluated by calculating L_2 relative errors at different grid levels ($|e_{\ell,2}|$) and evaluating the rates of convergence at each level. Three different grid levels are considered and obtained by uniformly subdividing the domain in triangular prisms that are further subdivided into three tetrahedra, thus ensuring that no obtuse angles are generated. For the one-dimensional problems we consider the domain $[0, 1] \times [0, 0.1] \times [0, 0.1]$. The coarsest mesh has 480 tetrahedra and the finest 30,720 tetrahedra. For the two-dimensional test the domain is $[0, 1] \times [0, 1] \times [0, 1]$ and the coarsest mesh has 3072 tetrahedra while the finest one is formed by 196,608 tetrahedra. A time step $\Delta t = 1 \times 10^{-3}$ s is used at the coarsest mesh of the one-dimensional tests and halved in passing to the next finer level. The CFL is kept constant at 0.29. In the two-dimensional example the time step is $\Delta t = 4 \times 10^{-3}$ s at the coarsest mesh (and halved in passing to the next finer level), and the CFL is equal to 0.33.

Table 1 shows the results obtained for the three tests relative to a final time $t^k = 0.$ s. The performance of the particular limiter is measured by the loss of accuracy observed with respect to the run where the limiter is not activated, reported in the same table for the LCD and LSM reconstructions, and named NLCD and NL_LSM, respectively. The scheme with the flux approximation calculated as the average of the four DUR candidates is also reported (AVG). Fig. 1 reports the convergence behavior of the various schemes for TEST2 in a log–log plot of the L_2 error vs. the mesh size. For comparison purposes the first and second order lines are reported.

The results show that DUR, MIN, LCD, and MLG achieve only first order accuracy, except for a few one-dimensional tests. LSM_EXTR achieves second order accuracy in TEST1A but reaches about 1.40 convergence rate for TEST2. LSM_BJ, together with AVG, achieves a rate approaching 1.80, the highest order across the different sample cases. Second order is always reached when no limiter is applied. The numerical results suggest that the extension to three dimensions of limiters that work satisfactorily in two-dimensions is not as straightforward as suggested by many authors. The LSM_BJ scheme appears to be the most robust among those considered in the simulations and it will be used in the present work.

3.4. The spatially variable time-splitting technique

Stability of the advection discretization is determined by the CFL constraint, while the dispersive step, being implicit, is not subject to stability restrictions. This allows for the use of different time steps sizes for advection (Δt_a) and dispersion (Δt_d). A finer advection time step together with a coarser dispersive time step

Table 1
Convergence behavior of the different finite volume schemes in the solution of purely advective sample tests

Method	ℓ	TEST1A		TEST1B		TEST2	
		$\lvert e_{\ell,2}\rvert$	Rate	$\lvert e_{\ell,2}\rvert$	Rate	$\lvert e_{\ell,2}\rvert$	Rate
DUR	1	9.50e − 3		3.84e − 2		1.29e − 1	
	2	5.09e − 3	0.90	1.90e − 2	1.01	6.56e − 2	0.97
	3	2.62e − 3	0.96	9.57e − 3	0.99	3.49e − 2	0.91
MIN	1	3.45e − 3		1.37e − 2		8.58e − 2	
	2	7.98e − 4	2.11	4.35e − 3	1.65	3.48e − 2	1.30
	3	2.06e − 4	1.95	1.27e − 3	1.78	2.03e − 2	0.78
AVG	1	3.90e − 3		1.16e − 2		7.38e − 2	
	2	1.01e − 3	1.95	3.51e − 3	1.72	2.42e − 2	1.61
	3	2.60e − 4	1.96	9.76e − 4	1.85	6.69e − 3	1.85
LCD	1	8.05e − 3		3.96e − 2		1.18e − 1	
	2	4.91e − 3	0.71	1.91e − 2	1.05	5.67e − 2	1.06
	3	2.61e − 3	0.91	9.45e − 3	1.01	2.70e − 2	1.07
NLCD	1	3.77e − 3		1.12e − 2		7.33e − 2	
	2	9.83e − 4	1.94	3.33e − 3	1.75	2.42e − 2	1.60
	3	2.50e − 4	1.97	9.17e − 4	1.86	6.67e − 3	1.86
MLG	1	1.11e − 2		3.61e − 2		1.10e − 1	
	2	5.20e − 3	1.09	1.74e − 2	1.05	5.28e − 2	1.06
	3	2.61e − 3	0.99	8.79e − 3	0.98	2.74e − 2	0.95
LSM_EXTR	1	4.14e − 3		1.28e − 2		8.60e − 2	
	2	1.03e − 3	2.01	3.66e − 3	1.81	3.31e − 2	1.38
	3	2.57e − 4	2.00	1.00e − 3	1.87	1.24e − 2	1.42
LSM_BJ	1	3.96e − 3		1.24e − 2		7.12e − 2	
	2	1.01e − 3	1.97	3.60e − 3	1.78	2.49e − 2	1.51
	3	2.55e − 4	1.98	1.00e − 3	1.85	7.24e − 3	1.78
NL_LSM	1	3.72e − 3		1.11e − 2		7.32e − 2	
	2	9.74e − 4	1.93	3.28e − 3	1.76	2.42e − 2	1.60
	3	2.46e − 4	1.98	9.02e − 4	1.86	6.67e − 3	1.86

($\Delta t_d = n_a \Delta t_a$, with n_a integer $\geqslant 1$) maintains the stability of the overall scheme if Δt_a is selected so that CFL < 1. The integer n_a is determined by accuracy considerations. This approach yields considerable CPU savings, if compared to the case with $\Delta t_d = \Delta t_a$, but introduces an error of the order of Δt_a, forcing the algorithm to become first order accurate [13]. Obviously, the desired accuracy can always be achieved by proper selection of n_a.

When dealing with spatially variable coefficients, a very small Δt_a is often forced by large velocities occurring on only a small portion of the domain. This suggests that a spatially variable time step size may accelerate the algorithm considerably [20]. For an easier description of such approach in this case, we consider, as an example, a domain Ω subdivided into two zones, Ω_1 and Ω_2, separated by an interface Γ_{12}. Let Δt_{a_i} denote the advective time step in zone i, $i = 1, 2$. The value of Δt_{a_1} is calculated to satisfy the CFL condition as if no spatially variable time steps were adopted, $\Delta t_{a_1} = \Delta t_a$, while $\Delta t_{a_2} = L_{a_1} \Delta t_{a_1}$ for some positive integer L_{a_1}. The diffusive time step is set to $\Delta t_d = n_a \Delta t_{a_2}$ for some positive integer n_a. Subdomain Ω_1 consists of those tetrahedra in which the CFL constraint yields a time step smaller than Δt_{a_2}, while subdomain Ω_2 contains the remaining cells. From a practical point of view, the integer L_{a_1} is chosen in such a way

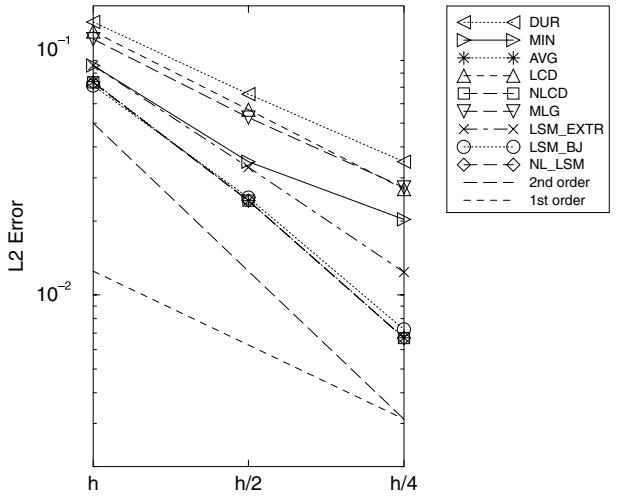

Fig. 1. Advection example: L_2 error vs spacing between adjacent nodes of the different meshes.

that approximately 80% or 90% of cells are located in Ω_2, thus attaining a considerable acceleration of the algorithm. The advection step proceeds by first applying the HRFV scheme within Ω_1 for L_{a_1} steps up to time $t^k + \Delta t_{a_2}$. For the tetrahedra belonging to Ω_1 and having a face on Γ_{12}, the advective flux on the boundary Γ_{12} is calculated by using the current solution in Ω_2. At time $t^k + \Delta t_{a_2}$, one advection step is performed in Ω_2 using the solution just calculated in the boundary elements of Ω_1. This terminates one full advection step over the entire domain Ω. The procedure above is then repeated n_a times until t^{k+1} is reached. Next, the dispersion step is carried out, obtaining the new solution c^{k+1}.

This procedure is easily generalized to $N_z > 2$ zones, as described in the following algorithm, where $\hat{F}$ and $\hat{G}$ denote the advective and dispersive numerical fluxes, respectively:

Algorithm 1 (*Time-splitting technique with spatially variable* Δt_{a_i}). For each time step, ($\Omega = \bigcup_{i=1}^{N_z} \Omega_i$, $L_{a_i} \Delta t_{a_i} = \Delta t_{a_{i+1}}$, $L_{a_{N_z}} = 1$, and $\Delta t_d = n_a \Delta t_{a_{N_z}}$, $i = 1, \ldots, N_z$) do:

- advection step:
  (1) $\phi_l c_l^{(0)} := \phi_l c_l^k$
  (2) DO $i_a = 0, n_a - 1$
    I. DO Ω_i, $i = 1, N_z$
      a. $\phi_l c_l^{(0)} := \phi_l c_l^{(i_a)}$
      b. SET $n_{a_i} = L_{a_i} \cdot L_{a_{i+1}} \cdots L_{a_{N_z}}$
      c. DO $j = 0, n_{a_i} - 1$

$$\phi_l c_l^{(j+1)} = \phi_l c_l^{(j)} + \Delta t_{a_i} \left[\hat{F}(c_l^{(j+1-\theta)}) \right] \tag{17}$$

      END DO
      d. $c_l^{(i_a+1)} := c_l^{(n_{a_i})}$

    END DO

  END DO
  (3) $\hat{c}_l^{k+1} := c_l^{(n_a)}$

- dispersion step:

$$\Delta t_{\mathrm{d}} = \Delta t = n_{\mathrm{a}} \Delta t_{N_z}$$

$$\phi_l c_l^{k+1} = \phi_l \hat{c}_l^{k+1} + \Delta t_{\mathrm{d}} \left[\hat{G}(c_l^{k+\theta}) \right]. \tag{18}$$

Continuity requires that, at the interfaces between different subregions, the concentration values in step (2d) of Algorithm 1 be calculated as:

$$\Delta t_{\mathrm{a}_{i+1}} \hat{F}(c_l^{n_{\mathrm{a}_i}}) = \sum_{j=0}^{n_{\mathrm{a}_i}-1} \Delta t_{\mathrm{a}_i} \hat{F}(c_l^{(j+1-\theta)})$$

so that global mass conservation in the sense of Eq. (7) is ensured [20].

4. Numerical results

In this section, we present and discuss a few numerical results obtained by the coupled flow and transport solver previously described. In all the simulations we use $\theta = 1$ and $n_a > 1$ together with a spatially variable advective time step. Other parameters of choice in the numerical scheme are reported in summary tables for each test case.

The initial guess of the Picard iteration is given by the extrapolated value:

$$(\psi_l, c_l)^{k+1,0} = (\psi_l, c_l)^{k+1,0} + v \frac{(t^{k+1} - t^k)}{(t^k - t^{k-1})} \left[(\psi_l, c_l)^k - (\psi_l, c_l)^{k-1} \right],$$

where $v \in [0, 1]$. Convergence of the iteration is achieved when

$$\| \boldsymbol{\psi}^{k+1,r+1} - \boldsymbol{\psi}^{k+1,r} \|_2 \leqslant \tau_\psi,$$

$$\| \mathbf{c}^{k+1,r+1} - \mathbf{c}^{k+1,r} \|_2 \leqslant \tau_c,$$

where τ_ψ and τ_c are two predefined tolerances. In case of non convergence, the time step is repeated with a smaller time step size using an empirical algorithm already tested in several problems [16,39]. Because of the linear convergence of Picard, the use of this technique ensures that the time step size is always maintained so that time accuracy is always better than the accuracy of the nonlinear system solution. Given Δt_{d} as selected by this procedure, the value of n_{a} is chosen so that the sought CFL constraint is satisfied in each of the regions Ω_i. In general, the number of subdomains is kept small as the distribution of CFL values is generally concentrated in only few regions. In our simulations a maximum of two subdomains has been used.

4.1. Elder's problem

The two-dimensional Elder problem has been used as a benchmark test case for two-dimensional density-dependent codes [1] and was extended to three spatial dimensions in [32]. The problem considers a free convection phenomenon, where the bulk fluid flow is driven purely by fluid density differences. The three-dimensional counterpart consists of a porous box with a square base of side 600 m and height 150 m. The box has the same cross-sections along the Cartesian axes as defined for the two-dimensional sketch (see Fig. 2). Salinity is held constant, in an areal extent, on the top and bottom of the porous box. The other parameters are given in Table 2.

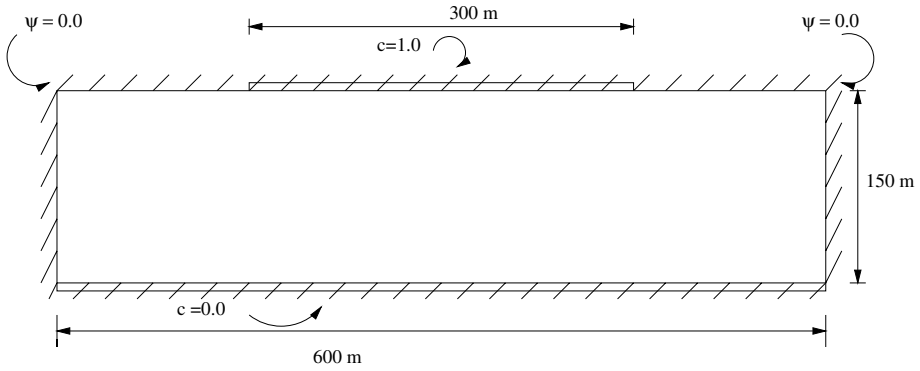

Fig. 2. Definition of Elder's problem as given in [1].

Table 2
Parameters for Elder's problem

Domain	Box with base 600 m × 600 m and height 150 m
Source location	Centered on the upper bound at $z = 150$ m at 150 m $\leqslant x \leqslant$ 450 m at 150 m $\leqslant y \leqslant$ 450 m
k	4.845e − 13 m^2
μ_0	86.4 kg/md
ρ_0	1000 kg/m^3
ϵ	0.2
ϵ'	0
ϕ	0.1
α_L, α_T	0 m
D_0	0.308016 m^2/d
K_{sx}	0.410654 m/d
K_{sy}	0.410654 m/d
K_{sz}	0.410654 m/d
S_s	9.8e − 3

The domain is discretized with a tetrahedral grid of 192,000 elements obtained by uniform subdivision of the domain in triangular prisms that are further subdivided into tetrahedra. A summary description of the grid and convergence parameters used is given in Table 3. The observed CFL number, with an imposed maximum value of 0.30, varies between 0.10 and 0.30.

The three-dimensional free convection process is similar to the two-dimensional counterpart, with some interesting new features. In the two-dimensional process, the solute enters the pure water initially by diffusion, increases its density, and a circulation process begins. The motion develops as a set of eddies forming, because of the solute density differences, at the two ends of the source. Small eddies of reverse circulation are associated with the end eddies, followed by a further set of eddies growing near the ends. This process continues in time until the end eddies merge into single large eddies.

Similar to the two-dimensional case, in three dimensions an up-welling salinity pattern can be found in the center of the box at later times. Fingers appear around the border of the intrusion area and 'blobs' grow down at the four corners. The quadratic pattern evolves into more complicated multicellular formations via a number of characteristic stages. More blobs appear until the salinity reaches the bottom. Then the structures begin to fuse and the pattern is completely reformed. At this point, a convection pattern with a characteristic diagonal 'star' forms as a result of the geometry of the square intrusion area. It is clear that the

Table 3
Elder's problem

BCs for flow	No flow Zero pressure head at the two upper corners
BCs for mass transport	$c = 0$ along the base and $c = 1$ at the source Zero concentration gradient elsewhere
IC for pressure head	Hydrostatic
IC for concentration	$c = 0$
Grid characteristics	192,000 tetrahedra, 390,400 faces
Nodal spacing	
Δx	15 m
Δy	15 m
Δz	7.5 m
Final time $T_{\max}$	7300 d
Δt_0	30 d
$\Delta t_{\min}$	10 d
$\Delta t_{\max}$	30 d
$maxit_1$	10
$maxit_2$	12
$maxit$	15
Convergence criteria:	τ_ψ, $\tau_c = 1.e-6$

Boundary (BC) and initial (IC) conditions. Grid characteristics. Convergence parameters.

final formations have a strong dependency on geometry [8]. The three-dimensional configuration after 2 and 4 years is shown in Fig. 3, where the fingers and the convective cells are clearly visible. Fig. 4 shows two horizontal sections at an elevation of 135 and 75 m for $t = 2$, 4 and 20 years. The computed salinity patterns agree well with the results obtained in the literature [8,32].

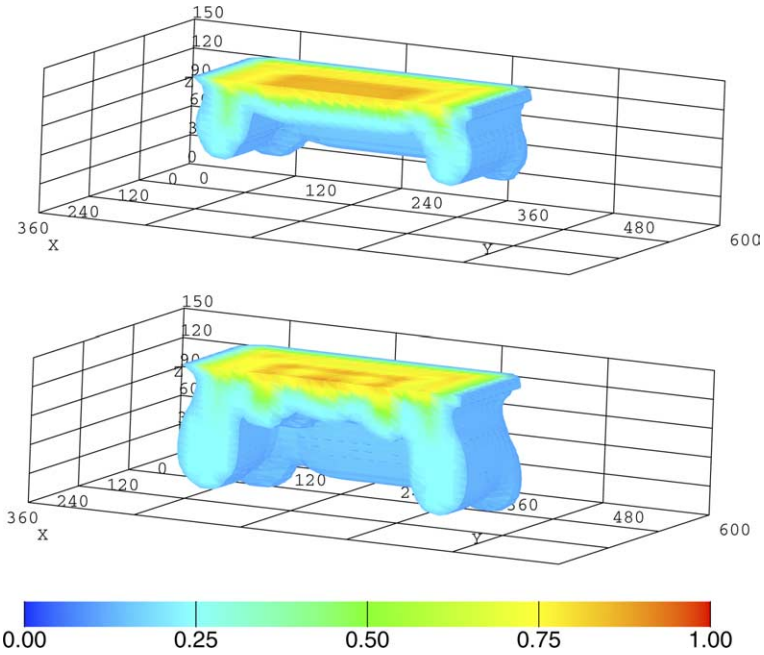

Fig. 3. Three-dimensional view of the 0.1 and 0.3 isosurfaces at times 2 (top) and 4 (bottom) years. The domain is cut at the middle of the x axis to emphasize the convective cells forming in the interior.

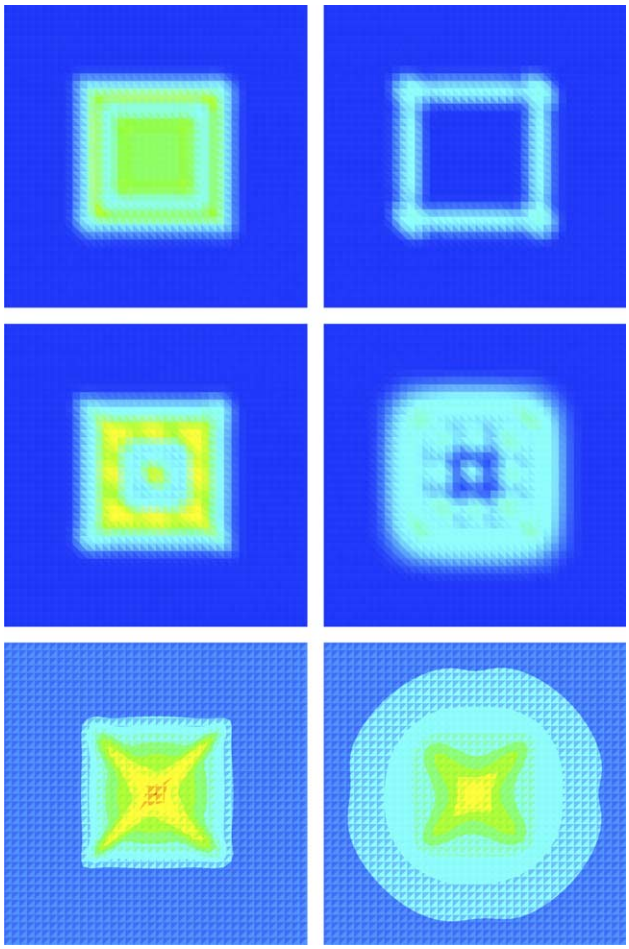

Fig. 4. Computed salinity pattern of the Elder problem at times 2 (top), 4 (middle) and 20 (bottom) years: horizontal views at an elevation of 135 m (left) and 75 m (right).

4.2. The saltpool problem

The saltpool problem has been proposed by [7] who describe a series of laboratory experiments that can be used as three-dimensional tests for benchmarking density driven porous media flow simulators. The experiments involve a cube (shown in Fig. 5) in which saltwater initially forms a bottom layer overlain by freshwater. A flow pattern is initiated by injecting a constant rate q of freshwater from one top corner and letting water out from the opposite corner. The flow pattern causes a time-dependent upconing of the saltwater due to lateral dispersion of the salty layer into the moving fresh water. Variation of the density difference between saltwater and freshwater is shown to have a significant influence on the flow pattern because of gravity effects.

An important outcome of the laboratory experiments is the breakthrough curves of salinity at the outflow hole. It is a challenging task to model these breakthrough behavior. Two different cases are studied with a maximum initial salt mass fraction ω (defined as the salt concentration c divided by the fluid density) of $\omega_{\max} = 1\%$ (low density, case 1) and $\omega_{\max} = 10\%$ (high density, case 2), respectively.

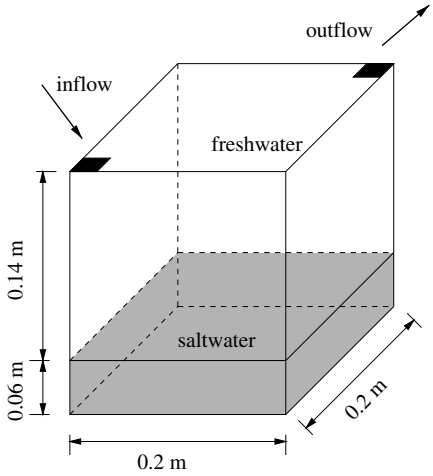

Fig. 5. Definition of the saltpool problem.

The saltpool problem has been modeled by various authors, see e.g. [10], with different success. The numerical investigation is complicated due to the extremely small values of the dispersivity coefficients and a large density contrast. The best agreements with the measurements have been achieved by [10], who have fitted some of the parameters to obtain an "optimal" numerical solution, in the sense of minimum differences between calculated and experimental breakthrough curves. They studied mesh convergence by using a hierarchy of regular hexahedral meshes up to eight grid levels. At the finest grid level, the total number of hexahedra is about 17 million. It was shown that extremely fine meshes are required to model test case 2 with sufficient accuracy.

In this example we reproduce the results of [10], whose adjusted parameters are summarized in Table 4. The initial condition for the salt concentration is expressed in terms of the salt mass fraction ω by a piecewise linear function defined as:

Table 4
Parameters for the saltpool problem

Domain	Case 1		Case 2
		Box of $0.2 \times 0.2 \times 0.2$ m	
k		11.94e − 10 m^2	
μ_0		1.002e − 3 kg/ms	
ρ_0		1000 kg/m^3	
ϵ	0.0076		0.0735
ϵ'	0.018		0.1909
ϕ		0.358	
α_L		1.2e − 3	
α_T		4.32e − 5	
D_0		10^{-10} m^2/s	
K_{sx}		0.011669 m/s	
K_{sy}		0.011669 m/s	
K_{sz}		0.011669 m/s	
S_s		0	

$$\omega(\vec{x},0)=\omega_{max}\begin{cases}1 & \text{if } z\leqslant z_m-\upsilon/2,\\ 1/2-(z-z_m)/\upsilon & \text{if } z_m-\upsilon/2\leqslant z\leqslant z_m+\upsilon/2,\\ 0 & \text{if } z_m+\upsilon/2\leqslant z,\end{cases} \tag{19}$$

where $z_m = V_m/\phi L$ denotes the vertical position of the initial mixing zone (V_m being the volume of saltwater recharged at the beginning of the experiment and L the length of the box), assuming a perfect horizontal interface between saltwater and freshwater, and υ is the width of the transition zone. Both parameters depend on the experiment. The inflow and outflow holes are at a constant rate q_N. Boundary conditions and other parameters pertaining to the numerical scheme are reported in Table 5.

In the simulations, the proposed approach with a spatially variable advective time step is used. More in detail, two subdomains, Ω_1 and Ω_2, have been identified in such a way that approximately 90% of the computational cells are located in Ω_2, where a relatively small n_a can be used, while the remaining ones are located in Ω_1, where the CFL condition forces a large value of n_{a_1}. For example, in the simulation of case 1 over a grid with 24,576 tetrahedra and with a diffusive time step $\Delta t_d = 17.525$ s, imposing that CFL=1 we obtain $n_a = 4$, $n_{a_1} = 138$ and the number of tetrahedra belonging to Ω_1 is equal to 1562. This means that 138 advective time steps are run on 1562 cells, followed by 1 advective time step on the remaining 23,014 cells. This procedure is repeated 4 times, and finally a dispersion step is taken. If no spatially variable advective time step was considered, 138×4 (that is 552) advective time steps should have been performed over all the 24,576 cells which would have been more than 14 times more expensive.

We consider two grid levels, corresponding to levels 4 and 5 on the hierarchy created in [10], and whose characteristics are described in Table 6. Simulations on finer grids would require parallelization of the code.

Table 5
Saltpool problem

	Case 1		Case 2
BCs for flow			
At the inflow hole	$q_N = 1.89\text{e}-6$ m^3/s		$q_N = 1.83\text{e}-6$ m^3/s
At the outflow hole	$q_N = -1.89\text{e}-6$ m^3/s		$q_N = -1.83\text{e}-6$ m^3/s
IC for pressure head		$\psi = 0$	
IC for concentration		$c = \omega/\rho$ (see Eq. (19))	
$\omega_{\max}$	1%		10%
V_m	8.64e − 4 m^3		8.9964 e − 4 m^3
υ		8e − 3 m	
Final time $T_{\max}$	8412 s		9594 s
Δt_0	17.525 s		4 s
$\Delta t_{\min}$	10 s		4 s
$\Delta t_{\max}$	17.525 s		9.9938 s
$maxit_1$	7		5
$maxit_2$	10		7
$maxit$	12		10
Convergence criteria		$\tau_\psi, \tau_c = 1.\text{e}-3$	

Boundary (BC) and Initial (IC) Conditions. Convergence parameters.

Table 6
Saltpool problem

Grid	Tetrahedra	Faces	Δx	Δy	Δz
1	24,576	50,688	0.0125 m	0.0125 m	0.0125 m
2	196,608	399,360	0.00625 m	0.00625 m	0.00625 m

Grid characteristics.

The results for the low (case 1) and high (case 2) density tests are presented in Figs. 6 and 7. A good approximation of the breakthrough curve for case 1 is obtained on the finest grid level 2. For the second test case a much finer grid would be necessary to achieve good accuracy. Nonetheless, the results obtained by means of the present approach are much closer to the experimental ones with respect to the corresponding curves obtained by [10]. In particular, the differences between the two numerical approaches are small at later times (after 4000 s) while between 0 and 4000 s the present results displays a better agreement to the measurements.

From the results of these simulations we can observe the following.

Remark 1. The choice of the appropriate discretization for advection is of great importance in this test case. Indeed, as it can be seen from Fig. 8, the extremum limiter seems to work satisfactorily in case 1 but gives disastrous results in case 2, as compared to the BJ limiter. The reason for this behavior can be explained by noting that the latter is less compressive, and thus better suited for linear advection–diffusion equations. This results in a more robust solution to small variations of the transversal dispersivity coefficient α_L, the parameter controlling diffusion of the saltwater into the moving freshwater layer. A limiter such as LSM_EXTR would be too compressive, tending to artificially sharpen the front thus hindering the effects of the transverse dispersivity coefficient.

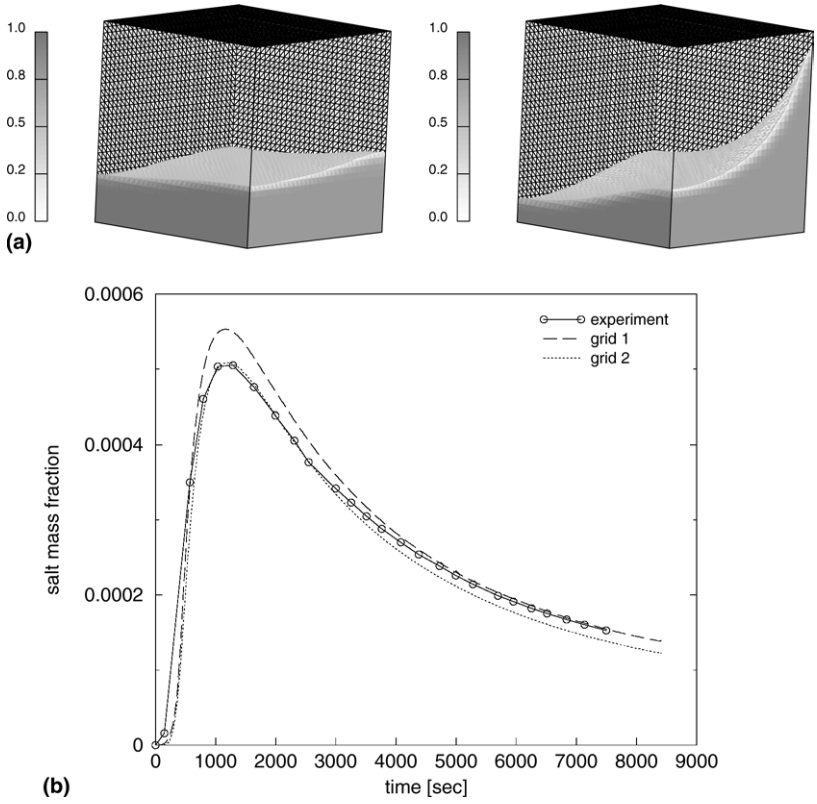

Fig. 6. Computational results of the saltpool problem for the low density case: (a) cross-sectional distributions at 150 (left) and 1000 (right) s for grid 2, (b) salinity breakthrough curves at the outlet obtained for grids 1 and 2.

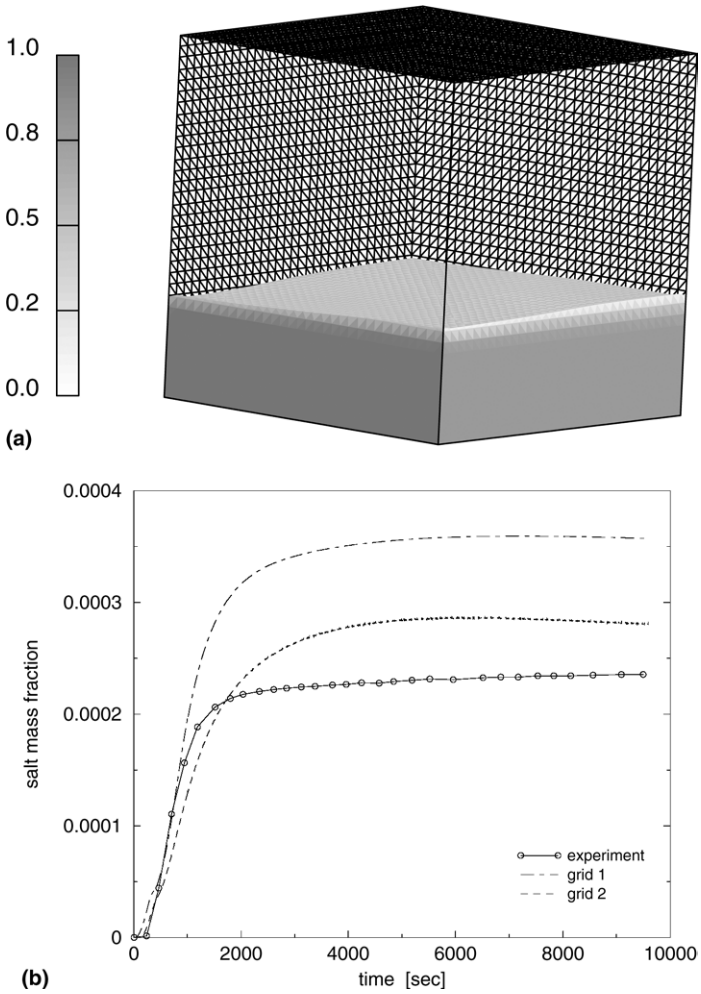

Fig. 7. Computational results of the saltpool problem for the high density case: (a) cross-sectional distributions at 2000 s for grid 2, (b) salinity breakthrough curves at the outlet obtained for grids 1 and 2.

Remark 2. The explicit nature of the time stepping scheme employed in the discretization of the advective component enforces a stability restriction on the advective time step size. This results in higher accuracy with respect to the discretization of the dispersion fluxes. We believe that this is the one of the reasons for the good performance of the scheme as compared to the approach of [10].

5. Conclusions

The numerical solution of high density convection dominated flows in three-dimensional porous media is a challenging task because of numerical difficulties and computational requirements. In this paper, we present and analyze an algorithm based on the combination of the MHFE scheme with the finite volume approach. The combination is based on the time splitting of the dispersive and advective components of the

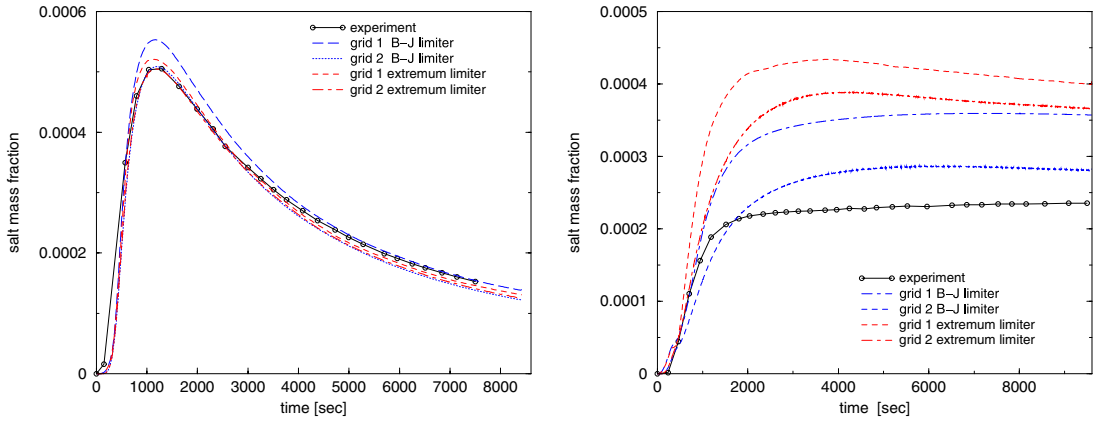

Fig. 8. Comparison between the BJ limiter and extremum limiter case 1 (left) and case 2 (right).

transport equation. The overall approach has been tested on two well known benchmark cases. The obtained solution accuracy and numerical efficiency well compare with respect to other schemes. In particular, the time accuracy and the robust limiter-reconstruction combination seem to be the key points for the success of the proposed numerical discretization. The fact that the time-splitting algorithm allows for the use of smaller time step sizes for the integration of the advective flux as compared to the dispersive flux is fundamental in capturing the fronts that develop in the case of large density differences. At the same time the selection of truly three-dimensional limiters that guarantee high accuracy also in the multidimensional case is crucial to obtain meaningful solutions on relatively coarse grids.

Acknowledgements

The authors would like to thank the anonymous reviewers for their helpful and thorough comments. This work has been partially supported by MURST-PRIN 2004019315 "Sviluppo di metodi numerici e algoritmi per applicazioni a problemi di fluidodinamica ambientale".

References

[1] C.I. Voss, W.R. Souza, Variable density flow and solute transport simulation of regional aquifers containing a narrow freshwater–saltwater transition zone, Water Resour. Res. 23 (10) (1987) 1851–1866.
[2] O. Kolditz, R. Ratke, H.J.G. Diersch, W. Zielke, Coupled groundwater flow and transport: 1. Verification of variable density flow and transport models, Adv. Water Resour. 21 (1) (1998) 27–46.
[3] P. Ackerer, A. Younes, R. Mose, Modeling variable density flow and solute transport in porous medium: 1. Numerical model and verification, Transp. Porous Media 35 (3) (1999) 345–373.
[4] G. Gambolati, M. Putti, C. Paniconi, Three-dimensional model of coupled density-dependent flow and miscible salt transport in groundwater, in: J. Bear, A.H.-D. Cheng, S. Sorek, D. Ouazar, I. Herrera (Eds.), Seawater Intrusion in Coastal Aquifers; Concepts, Methods and Practices, Kluwer Academic Publishers, Dordrecht, The Netherlands, 1999, pp. 315–362 (Chapter 10).
[5] R.A. Wooding, S.W. Tyler, I. White, Convection in groundwater below an evaporating salt lake, 1, Onset of instability, Water Resour. Res. 33 (6) (1997) 1199–1217.
[6] R.A. Wooding, S.W. Tyler, I. White, P.A. Anderson, Convection in groundwater below an evaporating salt lake, 2, Evolution of fingers or plumes, Water Resour. Res. 33 (6) (1997) 1219–1228.
[7] S. Oswald, Dichteströmungen in porösen medien: Dreidimensionale experimente und modellierung, Ph.D. thesis, ETH Zürich, 1999.

[8] H.-J. Diersch, O. Kolditz, Variable-density flow and transport in porous media: approaches and challenges, Adv. Water Resour. 25 (2002) 899–944.
[9] A. Mazzia, L. Bergamaschi, M. Putti, On the reliability of numerical solutions for density dependent flow and transport in groundwater, Transp. Porous Media 43 (1) (2001) 65–86.
[10] K. Johansen, W. Kinzelbach, S. Oswald, G. Wittum, The saltpool benchmark problem – numerical simulation of saltwater upconing in a porous medium, Adv. Water Resour. 25 (2002) 335–348.
[11] C. Cordes, M. Putti, Accuracy of Galerkin finite elements for the groundwater flow equation in two and three dimensional triangulations, Int. J. Numer. Meth. Eng. 52 (2001) 371–387.
[12] T. Russel, M. Wheeler, Finite element and finite difference methods for continuous flows in porous media, in: R. Ewing (Ed.), The Mathematics of Reservoir Simulation, SIAM, Philadelphia, PA, 1983, pp. 35–106.
[13] A. Mazzia, L. Bergamaschi, M. Putti, A time-splitting technique for advection–dispersion equation in groundwater, J. Comput. Phys. 157 (1) (2000) 181–198.
[14] A. Mazzia, L. Bergamaschi, C.N. Dawson, M. Putti, Godunov mixed methods on triangular grids for advection–dispersion equations, Comput. Geosci. 6 (2) (2002) 123–139.
[15] L. Bergamaschi, A. Mazzia, M. Putti, A time-splitting technique for the solution of density dependent flow and transport in groundwater, in: L.R. Bentley et al. (Eds.), Computational Methods in Water Resources, Balkema, Rotterdam, 2000, pp. 75–82.
[16] A. Mazzia, M. Putti, Mixed-finite element and finite volume discretization for heavy brine solutions in groundwater, J. Comput. Appl. Math. 147 (1) (2002) 191–213.
[17] C.T. Simmons, K.A. Narayan, R.A. Wooding, On a test case for density-dependent groundwater flow and solute transport model: the salt lake problem, Water Resour. Res. 35 (12) (1999) 3607–3620.
[18] S.M. Hassanizadeh, T. Leijnse, A non-linear theory of high-concentration-gradient dispersion in porous media, Adv. Water Resour. 18 (4) (1995) 203–215.
[19] S.M. Hassanizadeh, T. Leijnse, On the modeling of brine transport in porous media, Water Resour. Res. 24 (3) (1988) 321–330.
[20] C.N. Dawson, High resolution upwind-mixed finite element methods for advection diffusion equations with variable time-stepping, Numer. Meth. PDE 11 (1995) 525–538.
[21] T.J. Barth, D.C. Jespersen, The design and application of upwind schemes on unstructured meshes, AIAA paper 89-0366, 1989, pp. 1–12.
[22] A. Mazzia, M. Putti, Investigation of extension of high order finite volume schemes from triangles to tetrahedra, in: D.K.R. Herbin (Ed.), Finite Volumes for Complex Applications III, Problems and Perspectives, Hermes Penton Science, London, 2002, pp. 413–420.
[23] E. Godlewski, P. Raviart, Numerical Approximation of Hyperbolic Systems of Conservation Laws, Springer, New York, 1996.
[24] L.J. Durlofsky, B. Engquist, S. Osher, Triangle based adaptive stencils for the solution of hyperbolic conservation laws, J. Comput. Phys. 98 (1992) 64–73.
[25] M.E. Hubbard, Multidimensional slope limiters for MUSCL-type Finite Volume schemes on unstructured grids, J. Comput. Phys. 155 (1) (1999) 54–74.
[26] P. Batten, C. Lambert, D. Causon, Positively conservative high-resolution convection schemes for unstructured meshes, Int. J. Numer. Meth. Eng. 39 (1996) 1821–1838.
[27] H. Yan, G. Urbin, D. Knight, A.A. Zheltovodov, Compressible large eddy simulation using unstructured grid: supersonic boundary layer and compression ramps, in: 10th International Conference on Methods of Aerophysical Research, Novosibirsk, Russia, 2000, pp. 1–8.
[28] Y. Coudiere, J.-P. Vila, P. Villedieu, Convergence rate of a finite volume scheme for a two dimensional convection–diffusion problem, Math. Model. Numer. Anal. 33 (3) (1999) 493–516.
[29] E. Bertolazzi, G. Manzini, A cell-centered second-order accurate finite volume method for convection–diffusion problems in unstructured meshes, Math. Model. Meth. Appl. Sci. 14 (8) (2004) 1235–1260.
[30] A. Harten, S. Osher, B. Engquist, S.R. Chakravarthy, Some results on uniformly high-order accurate essentially nonoscillatory schemes, Appl. Numer. Math. 2 (1986) 347–377.
[31] A. Harten, B. Engquist, S.R. Chakravarthy, Uniformly high-order accurate essentially nonoscillatory schemes. iii, J. Comput. Phys. 71 (1987) 231–303.
[32] H.-J.G. Diersch, O. Kolditz, Coupled groundwater flow and transport: 2. Thermohaline and 3D convection systems, Adv. Water Resour. 21 (1998) 401–425.
[33] J. Bear, Hydraulics of Groundwater, McGraw-Hill, New York, 1979.
[34] G. Dagan, Theory of solute transport by groundwater, Annu. Rev. Fluid Mech. 19 (1987) 183–215.
[35] L. Bergamaschi, M. Putti, Mixed finite elements and Newton-like linearization for the solution of Richard's equation, Int. J. Numer. Meth. Eng. 45 (8) (1999) 1025–1046.
[36] A. Mazzia, M. Putti, Three dimensional godunov mixed methods on tetrahedra for the advection–dispersion equation, in: W.G.G.S.M. Hassanizadeh, R.J. Schotting, G. Pinder (Eds.), Computational Methods in Water Resources, Developments in Water Resources, 47, vol. 1, Elsevier, Amsterdam, 2002, pp. 381–388.

[37] F. Brezzi, M. Fortin, Mixed and Hybrid Finite Element Methods, Springer, Berlin, 1991.
[38] X.-D. Liu, A maximum principle satisfying modification of triangle based adaptive stencils for the solution of scalar hyperbolic conservation laws, SIAM J. Numer. Anal. 30 (3) (1993) 701–716.
[39] C.M. D'Haese, M. Putti, C. Paniconi, N.E. Verhoest, F.D. Troch, Assessment of initial solution estimates and adaptive vs. heuristic time stepping for variably saturated flow, in: C. Miller et al. (Eds.), Computational Methods in Water Resources, vol. 1, Elsevier, Amsterdam, 2004, pp. 545–556.